

# Analysis of the Drive of the Electric Vehicle with Six-Phase Induction Motor

Research paper

Jacek Listwan<sup>\*</sup>, Piotr Oleszczyszyn

Department of Electrical Machines, Drives and Measurements, Faculty of Electrical Engineering, Wrocław University of Science and Technology, Wrocław, Poland

Received: 04 April 2023; Accepted: 12 July 2023

**Abstract:** The article presents the analysis of the drive system of the electric vehicle with a six-phase induction motor. The mathematical models of the six-phase induction motor and model reference adaptive system (MRAS) estimator are presented, and the description of the voltage source inverter, space vector modulator and bidirectional buck–boost converter is shown. The direct field-oriented control (DFOC) system and the direct torque control with space vector modulation (DTC-SVM) system are analysed. Results of simulation studies of these control methods and comparative analysis are shown. The DTC-SVM method is selected as the method with the best properties, and a full model of the electric vehicle drive system is built using this method. The detailed description of the drive system of the electric vehicle with a six-phase induction motor and DTC-SVM control system and the results of simulation tests for this drive system are presented. The aim of the authors and an element of novelty is to develop and test a drive system for an electric vehicle with a six-phase induction motor, adaptive speed estimator and extensive space vector modulator.

**Keywords:** electric vehicle • six-phase squirrel-cage induction motor • direct field-oriented control • direct torque control with space vector modulation • sensorless drives

## 1. Introduction

The first electric vehicles appeared on the roads in the 1830s. Due to the insufficient state of knowledge in the fields of power electronics, electricity storage and electrical machines, they were not a convenient means of transport. In the 21<sup>st</sup> century, the development of these fields allowed electric vehicles to compete with combustion engines. Their range, power and charging speed have increased to a level that ensures comfortable use of the car. Thanks to high-efficiency systems and the parallel development of renewable energy sources, the propulsion of electric vehicles not only begins to exceed the parameters of combustion vehicles but also enables emission-free driving. Drive systems with electric motors are used and developed to this day, which allows the transfer of known control methods to the drive systems with electric vehicles (Guziński and Adamowicz, 2013; Łebkowski, 2017; Sztáfrowski and Kaznowski, 2021; Zachariasz and Dybkowski, 2014).

In this study, the drive system with a six-phase squirrel-cage induction motor has been investigated. Comparing a six-phase and a three-phase induction motor with the same rated power, rotational speed, number of pole pairs and supply voltage, the following advantages of multiphase motor can be distinguished: the nominal currents of a six-phase induction motor have half the amplitudes in comparison with a three-phase motor; due to the lower currents in the multiphase motor, the required parameters of switchgear and protection equipment are reduced; due to the greater number of voltage vectors generated by the multiphase inverter, the vector modulator for a multiphase motor is more extensive, and therefore, the multiphase motor generates less electromagnetic torque pulsations; due to the greater number of phases, the multiphase motor reliability is higher (Che et al., 2014; Frikha et al., 2023; Levi et al., 2007; Listwan, 2019; Listwan and Pierkowski, 2016; Munim et al., 2017; Strankowski et al., 2019; Taha et al., 2022).

\* Email: jacek.listwan@pwr.edu.pl

The reliability of a multiphase motor is higher than that of a three-phase motor because in the event of phase losses, e.g., due to a burnt coil, mechanical damage of the cable or loss of connection, the six-phase motor can still run. If even three phases are lost, it is possible to control the motor to run as a three-phase motor. This allows to ensure smooth operation of the motor, only with partial power due to the limited maximum currents that could flow through the stator windings. The reliability can be critical in electric vehicle propulsion as vehicle failure typically occurs far from home and an accessible workshop. Powertrain systems with six-phase electric motors can be used both in more luxurious cars as a competitive advantage and also in vehicles for special applications. In the first case, this advantage can be used as a marketing advantage, which would raise the attractiveness and price of the product. Considering the special applications of vehicles, that is, places such as mines, dense forests or mountainous terrain, it is difficult to repair the vehicle in case of a malfunction in the drivetrain. It is necessary to have specialised tools or to transport the damaged vehicle to a more accessible location. In this case, the ability to reach the repair point on one's own is an advantage.

The aim of the authors and an element of novelty is to develop and test a drive system for an electric vehicle with a six-phase induction motor, adaptive speed estimator and extensive space vector modulator. In this article, the two structures of the vector control of the six-phase induction motor are described: the direct field-oriented control and the direct torque control with a space vector modulator (Frikha et al., 2023; Levi et al., 2007; Orłowska-Kowalska, 2003; Taha et al., 2022). Comparative studies of selected structures were carried out, and one method with the best properties was selected for thorough analysis. This method was selected to build a full model of the electric vehicle drive system, simulation tests were performed for this method and the results of simulation tests were presented.

This article is divided into nine sections. First in Section I, introduction is presented. Next in Section II, the mathematical model of the six-phase induction motor is described. The six-phase VSI and the space vector modulator are presented in Section III. In Section IV, the description of the model reference adaptive system (MRAS<sup>F</sup>) estimator is presented. The battery and boost converter are discussed in Section V. Section VI deals with the description of the direct field-oriented control system and direct torque control system with space vector modulator. Simulation results are presented and discussed in Sections VII and VIII. The article is finished with conclusions.

## 2. Mathematical Model of the Six-Phase Induction Motor

The mathematical model of the six-phase squirrel-cage induction motor has been formulated based on the commonly used simplifying assumptions (Levi et al., 2007; Listwan, 2019; Listwan and Pieńkowski, 2016). The mathematical model of the six-phase induction motor in the phase coordinate system is described by differential equations with coefficients changing as a function of the angle of rotor rotation. Equations with constant coefficients can be obtained by the use the appropriate transformation of phase variables (Frikha et al., 2023; Levi et al., 2007; Listwan, 2019; Strankowski et al., 2019).

After applying the transformation matrix [C]:

$$[C] = \frac{2}{6} \begin{bmatrix} 1 & \cos\alpha & \cos2\alpha & \cos3\alpha & \cos4\alpha & \cos5\alpha \\ 0 & \sin\alpha & \sin2\alpha & \sin3\alpha & \sin4\alpha & \sin5\alpha \\ 1 & \cos2\alpha & \cos4\alpha & \cos6\alpha & \cos8\alpha & \cos10\alpha \\ 0 & \sin2\alpha & \sin4\alpha & \sin6\alpha & \sin8\alpha & \sin10\alpha \\ \frac{1}{\sqrt{2}} & \frac{1}{\sqrt{2}} & \frac{1}{\sqrt{2}} & \frac{1}{\sqrt{2}} & \frac{1}{\sqrt{2}} & \frac{1}{\sqrt{2}} \\ \frac{1}{\sqrt{2}} & -\frac{1}{\sqrt{2}} & \frac{1}{\sqrt{2}} & -\frac{1}{\sqrt{2}} & \frac{1}{\sqrt{2}} & -\frac{1}{\sqrt{2}} \end{bmatrix} \quad (1)$$

( $\alpha=2\pi/n$  is the electrical angle between the axes of the machine phase windings); the stator and rotor phase variables of the six-phase induction motor can be transformed to variables considered in the transformed coordinate systems: the stationary coordinate system  $\alpha\text{-}\beta$ , the additional coordinate system  $z_1\text{-}z_2$  and the system of zero components.

The components in the  $\alpha$ - $\beta$  coordinate system can be transformed afterwards to the x-y coordinate system, which rotates at arbitrary angular speed  $\omega_k$  after applying the transformation matrix  $[D]$ , as presented as follows:

$$[D] = [D(\vartheta_k)] = \begin{bmatrix} \cos\vartheta_k & \sin\vartheta_k & & & & \\ -\sin\vartheta_k & \cos\vartheta_k & & & & \\ & & 1 & & & \\ & & & \dots & & \\ & & & & & 1 \end{bmatrix} \quad (2)$$

where  $\vartheta_k = \int_0^t \omega_k dt$ .

The transformations of the electromagnetic variables of the stator and rotor of the multiphase motor to a common general x-y coordinate system rotating at arbitrary angular speed  $\omega_k$  and transformations to other additional coordinate systems, marked with the index z or 0, can be represented by the example relations given as follows:

$$\begin{bmatrix} u_{sx} \\ u_{sy} \\ u_{sz1} \\ u_{sz2} \\ u_{s01} \\ u_{s02} \end{bmatrix} = [D] \cdot \begin{bmatrix} u_{s\alpha} \\ u_{s\beta} \\ u_{sz1} \\ u_{sz2} \\ u_{s01} \\ u_{s02} \end{bmatrix} = [D][C] \cdot \begin{bmatrix} u_{s1} \\ u_{s2} \\ u_{s3} \\ u_{s4} \\ u_{s5} \\ u_{s6} \end{bmatrix} \quad (3)$$

These relationships were formulated for the variables expressed by the motor voltages defined in the phase coordinates and for transformed variables. The same transformations are valid for other electromagnetic variables of the stator and rotor of the six-phase induction motor currents and fluxes.

In the case of a six-phase coordinate system, three independent coordinate systems are obtained after transformation: the x-y coordinate system, the z1-z2 coordinate system and the system of two zero components. The components in the z1-z2 coordinate system do not generate the electromagnetic torque, but they affect to the values of the phase currents of the stator and, consequently, the losses in the motor. Therefore, these components cannot be omitted in further analysis. The zero components can be omitted because in the case of a star connection of the motor, the values of these components are always equal to zero.

The mathematical model of the motor takes the following form (Frikha et al., 2023; Levi et al., 2007; Listwan, 2019; Listwan and Pieńkowski, 2016):

- The differential equations of the stator circuit:

$$u_{sx} = R_s \cdot i_{sx} - \omega_k \psi_{sy} + \frac{d\psi_{sx}}{dt} \quad (4)$$

$$u_{sy} = R_s \cdot i_{sy} + \omega_k \psi_{sx} + \frac{d\psi_{sy}}{dt} \quad (5)$$

- The differential equations of the rotor circuit:

$$0 = R_r \cdot i_{rx} - (\omega_k - \omega_e) \psi_{ry} + \frac{d\psi_{rx}}{dt} \quad (6)$$

$$0 = R_r \cdot i_{ry} + (\omega_k - \omega_e) \psi_{rx} + \frac{d\psi_{ry}}{dt} \quad (7)$$

- The differential equations of the stator circuit in the additional  $z1$ - $z2$  coordinate system:

$$u_{sz1} = R_s \cdot i_{sz1} + \frac{d\psi_{sz1}}{dt} \quad (8)$$

$$u_{sz2} = R_s \cdot i_{sz2} + \frac{d\psi_{sz2}}{dt} \quad (9)$$

- The equation of the motor electromagnetic torque:

$$T_e = \frac{6}{2} \cdot p_b \cdot \frac{L_m}{L_r} \cdot (\psi_{rx} \cdot i_{sy} - \psi_{ry} \cdot i_{sx}) \quad (10)$$

where  $u$  is the voltage;  $i$  is the current;  $u_{sx}$ ,  $u_{sy}$ ,  $u_{sz1}$  and  $u_{sz2}$  are the components of the stator voltage vectors in the  $x$ - $y$  and  $z1$ - $z2$  coordinate system;  $i_{sx}$ ,  $i_{sy}$ ,  $i_{rx}$ ,  $i_{ry}$ ,  $i_{sz1}$  and  $i_{sz2}$  are the components of the stator and rotor current vectors in the  $x$ - $y$  and  $z1$ - $z2$  coordinate system;  $\psi_{sx}$ ,  $\psi_{sy}$ ,  $\psi_{rx}$ ,  $\psi_{ry}$ ,  $\psi_{sz1}$  and  $\psi_{sz2}$  are the components of the stator and rotor fluxes vectors in the  $x$ - $y$  and  $z1$ - $z2$  coordinate system;  $\omega_m$  is the mechanical angular speed of the motor;  $p_b$  is the number of pole pairs;  $\omega_e = \omega_m \cdot p_b$  is the electrical angular speed of the motor;  $\omega_k$  is the arbitrary angular speed of the coordinate system relative to the stator;  $L_r$  is the self-inductance of the rotor windings;  $L_m$  is the mutual inductance;  $R_s$  and  $R_r$  are the stator and rotor winding resistances; and  $T_e$  is the electromagnetic torque.

### 3. Six-Phase Voltage Source Inverter and Space Vector Modulator

The device that changes the DC voltage into AC voltage is an voltage source inverter (VSI) consisting of twelve IGBT transistors. It is considered that the six-phase induction motor is supplied by the two-level six-phase VSI (Bodo et al., 2017; Diab et al., 2016; Frikha et al., 2023; Levi et al., 2007; Listwan and Pierkowski, 2016; Taha et al., 2022). The scheme of the six-phase VSI is shown in Figure 1.

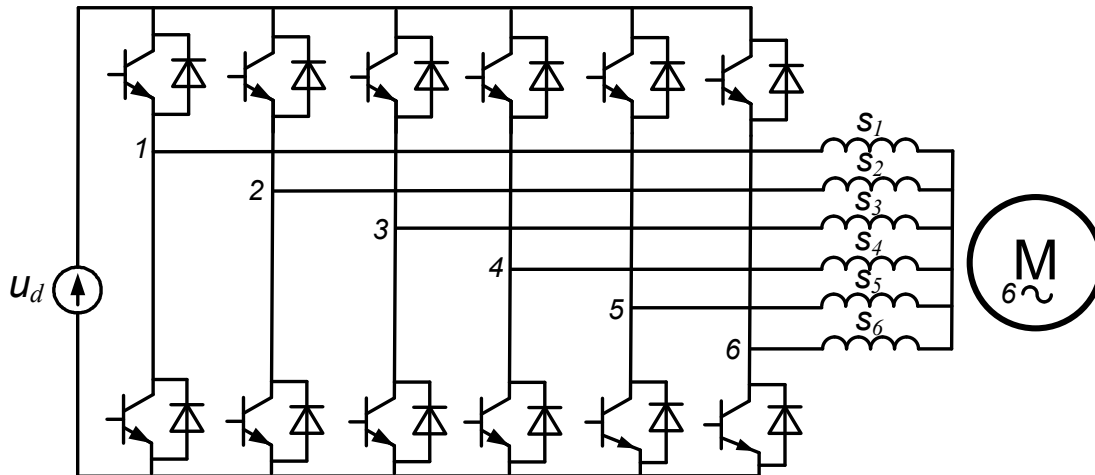


**Fig. 1.** Scheme of the six-phase voltage source inverter.

The two transistors are assigned to each phase—upper and lower. The control system switches them on alternately, so it is not possible to switch them on at the same time, which would lead to a short circuit of both battery poles. The control signals for the transistors are generated by the space vector modulator.

For a six-phase motor, it is possible to generate 64 vectors, ten of which are zero vectors. Voltage space vectors generated by the six-phase voltage source inverter in the stationary coordinate system  $\alpha$ - $\beta$  and in the additional coordinate system  $z1$ - $z2$  are determined with using the following equations (Listwan and Pierkowski, 2016; Novotny and Lipo, 1996):

$$\underline{u}_{s\alpha\beta} = u_{s\alpha} = ju_{s\beta} = \frac{1}{3}(S_1 + aS_2 + a^2S_3 + a^3S_4 + a^4S_5 + a^5S_6) \cdot u_d \tag{11}$$

$$\underline{u}_{s1z2} = u_{s1} + ju_{s2} = \frac{1}{3}(S_1 + a^2S_2 + a^4S_3 + a^6S_4 + a^2S_5 + a^4S_6) \cdot u_d \tag{12}$$

where  $\alpha = \exp(j2\pi/6)$ ;  $S_1, \dots, S_6$  are the switching functions of the six-phase voltage source inverter switches ( $S_i=0$  or  $S_i=1, i=1, \dots, 6$ ); and  $u_d$  is the voltage in the DC link of the voltage source inverter.

The voltage space vectors generated by the six-phase voltage source inverter in the  $\alpha\text{-}\beta$  coordinate system are shown in Figure 2 (Frikha et al., 2023; Levi et al., 2007; Listwan and Pieńkowski, 2016).

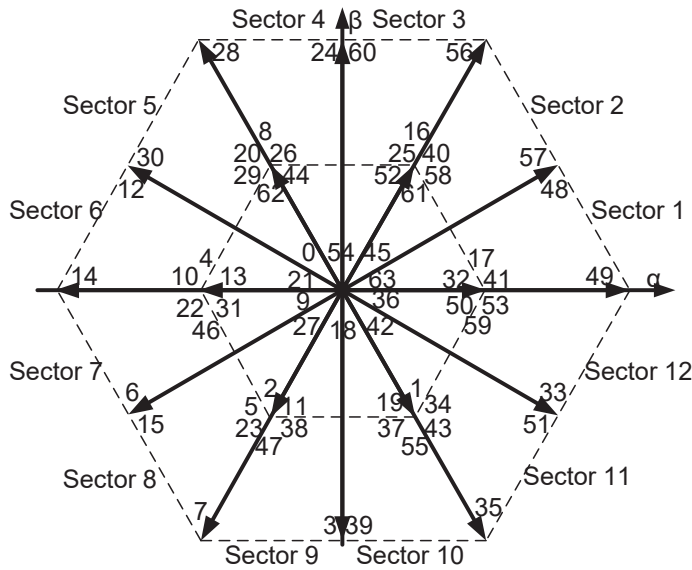


Fig. 2. Voltage space vectors generated by the six-phase VSI in the  $\alpha\text{-}\beta$  coordinate system.

It is not necessary to use all vectors for proper control. Some of them overlap with each other, and they are distinguished from each other by the switching state of the transistors of the inverter. It is possible to implement the control method with a division into six sectors, as in the three-phase system and with a division into twelve sectors. The larger number of vectors increases the number of transitions between the sectors, which reduces the pulsation of the motor torque and more accurate operation of the control system. The modulator using the division into twelve vectors has been applied in the analysed control systems. The use of an SVM ensures that the switching frequency of the transistors is constant.

The vector modulator is the system that, based on the set values of the stator voltage vector components in the  $\alpha\text{-}\beta$  coordinate system, generates control signals for the transistor of the voltage source inverter. The simulation model of the space vector modulator is presented in Figure 3.

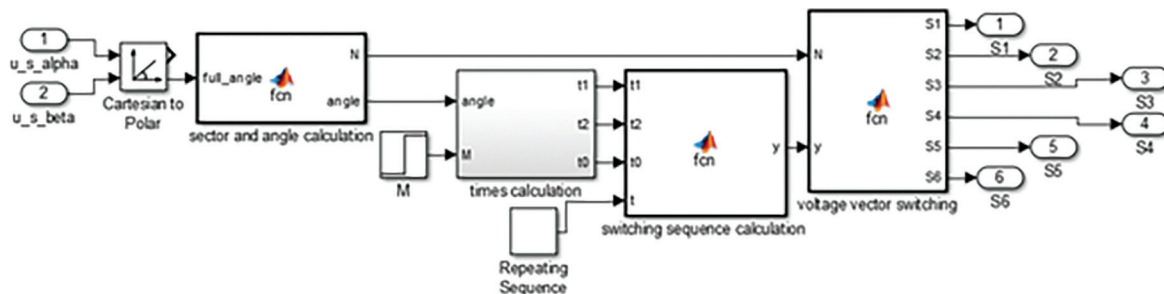


Fig. 3. Simulation model of the space vector modulator.

At the beginning, the stator voltage vector is determined, and based on its angle, the sector in which the vector is located is determined. Depending on the exact position of the voltage vector in this sector, the switching times of the voltage vectors leading the stator current vector ( $t_1$ ) and lagging behind it ( $t_2$ ) and the switching time of the zero vector ( $t_0$ ) are calculated. Based on the set times and the current sector, it is possible to determine the activation states of the transistor of the inverter.

The switching times of the transistors were determined based on the following formulas (Levi et al., 2007; Listwan and Pierkowski, 2016):

$$t_1 = \frac{2\sqrt{3}}{\pi} MT_s \sin\left(\frac{\pi}{6} - \alpha_{ref}\right) \quad (13)$$

$$t_2 = \frac{2\sqrt{3}}{\pi} MT_s \sin(\alpha_{ref}) \quad (14)$$

$$t_0 = T_s - (t_1 + t_2) \quad (15)$$

where  $t_1$  is the switching time of the leading vector;  $t_2$  is the switching time of the delay vector;  $t_0$  is the switching time of the zero vector;  $M$  is the coefficient of the modulation depth;  $T_s$  is the sampling time; and  $\alpha_{ref}$  is the angle of the reference voltage vector.

The modulator using the twelve voltage vectors with the highest magnitudes dividing the vector plane into twelve sectors has been applied in the analysed control systems. For the assumed position of the set stator voltage vector in Sector 1, the modulation algorithm is described by the following equation:

$$u_{sref} \cdot T_s = u_{49} \cdot t_1 + u_{48} \cdot t_2 + u_{40} \cdot t_0 \quad (16)$$

## 4. MRAS<sup>F</sup> Estimator

The MRAS<sup>F</sup>-type estimator was used to calculate the rotor flux vector and the angular speed of the motor. The use of the speed estimator allows increasing the reliability of the drive system in the event of damage to the speed sensors in the vehicle (Bednarz and Dybkowski, 2019; Korzonek et al., 2019).

The MRAS<sup>F</sup> estimator consists of a voltage model of the rotor flux estimator and current model of the rotor flux estimator. The flux vector is determined based on the first system and the motor speed based on comparing the values from both estimators and using the adaptation mechanism with a proportional—integral controller. The second structure is tuneable during operation based on the estimated speed (Bednarz and Dybkowski, 2019; Korzonek et al., 2019).

The scheme of the estimator of the rotor flux and motor speed is presented in Figure 4.

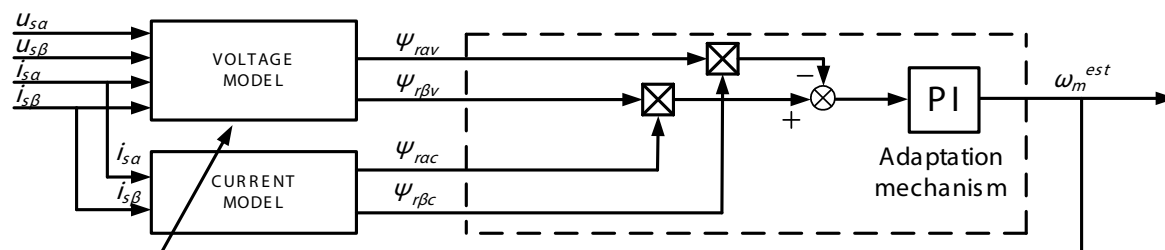


Fig. 4. Scheme of the estimator of the rotor flux and the motor speed.

The voltage model of the rotor flux estimator has been modelled using the relationships describing this motor variable in both axes of the  $\alpha$ - $\beta$  coordinate system. The stator circuit model has been described as follows (Bednarz and Dybkowski, 2019; Korzonek et al., 2019):

$$\frac{d}{dt}\psi_{r\alpha v} = \frac{L_r}{L_m} \left( u_{s\alpha} - R_s i_{s\alpha} - \sigma L_s \frac{d}{dt} i_{s\alpha} \right) \quad (17)$$

$$\frac{d}{dt}\psi_{r\beta v} = \frac{L_r}{L_m} \left( u_{s\beta} - R_s i_{s\beta} - \sigma L_s \frac{d}{dt} i_{s\beta} \right) \quad (18)$$

The rotor flux was also determined based on the current model, and the obtained values from both models were used to calculate the motor rotational speed (Bednarz and Dybkowski, 2019; Korzonek et al., 2019):

$$\frac{d}{dt}\psi_{r\alpha c} = \frac{R_r}{L_r} (L_m i_{s\alpha} - \psi_{r\alpha}) - \psi_{r\beta} \omega_{e\_est} \quad (19)$$

$$\frac{d}{dt}\psi_{r\beta c} = \frac{R_r}{L_r} (L_m i_{s\beta} - \psi_{r\beta}) + \psi_{r\alpha} \omega_{e\_est} \quad (20)$$

$$\omega_{e\_est} = K_p (\psi_{r\alpha c} \psi_{r\beta v} - \psi_{r\alpha v} \psi_{r\beta c}) + \frac{1}{T_i} \int_0^t (\psi_{r\alpha c} \psi_{r\beta v} - \psi_{r\alpha v} \psi_{r\beta c}) dt \quad (21)$$

where  $\psi_{r\alpha c}$  and  $\psi_{r\beta c}$  are the estimated components of the rotor flux vector obtained from the current model in the  $\alpha$ - $\beta$  coordinate system;  $\psi_{r\alpha v}$  and  $\psi_{r\beta v}$  are the estimated components of the rotor flux vector obtained from the voltage model in the  $\alpha$ - $\beta$  coordinate system;  $\omega_{e\_est}$  is the electrical estimated speed of the motor; and  $K_p$  and  $T_i$  are parameters of the proportional and integral parts of the PI controller.

The magnitude of the stator flux vector is determined from the following equation:

$$\psi_s = \frac{L_m}{L_r} \psi_r + \sigma L_s i_s \quad (22)$$

The rotor flux determined from the voltage model is used for computing the stator flux.

## 5. Battery and Bidirectional Buck–Boost Converter

In the tested system, the battery was designed based on the actual battery found in Nissan Leaf vehicles (Hayes and Davis, 2014). The parameters that were entered into MATLAB-Simulink software included the rated and maximum voltage, maximum battery capacity and internal resistance. For research purposes, the entered data were modified as follows: the maximum battery capacity was reduced from 67Ah to 2Ah, and the internal resistance of the cells was increased by an order of magnitude. With these changes, the negative effects of battery discharge and the influence of the cells' internal resistance on voltage were enhanced. This made it possible to test the bidirectional buck–boost converter under conditions heavier than the intended operating conditions. The stabilised DC voltage from the bidirectional buck–boost converter supplies the 6-phase VSI in the analysed control structures. The simulation models of the battery and bidirectional buck–boost converter were modelled with the use of blocks from the Sim Power System library to reproduce the real drive system as faithfully as possible. The obtained results are therefore more similar to the results obtained on a real object. The voltage value in the converter was stabilised, which had an impact on the proper operation of the analysed control structures. The simulation model of the battery and bidirectional buck–boost converter is shown in Figure 5.

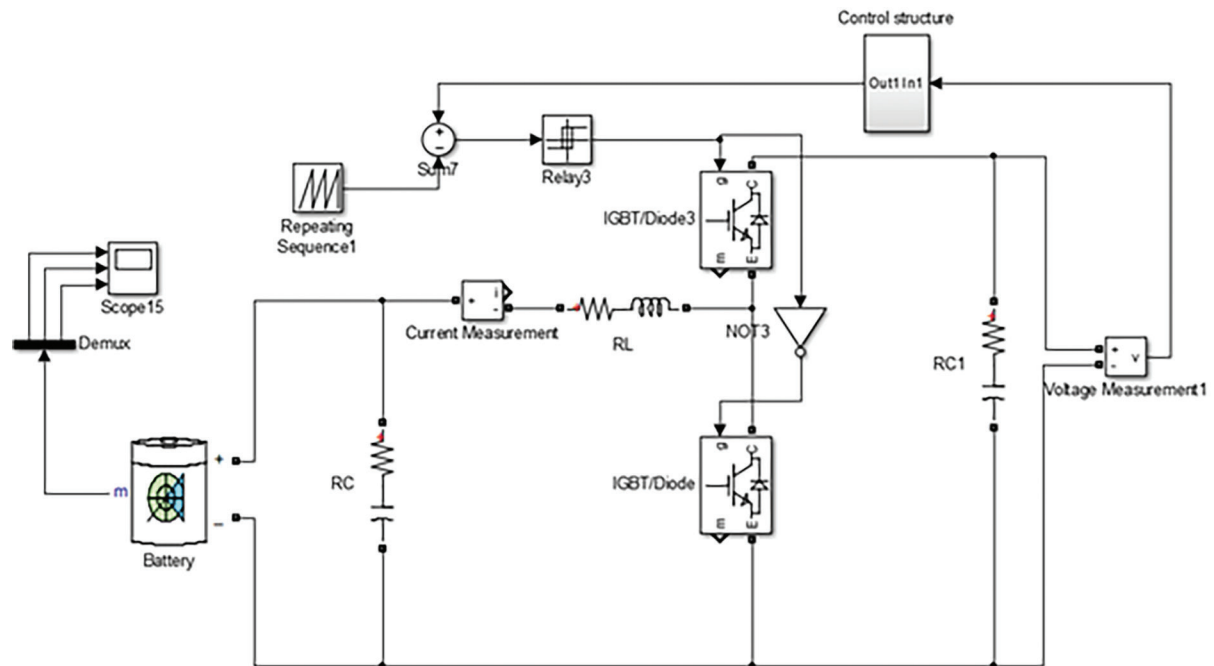


Fig. 5. Simulation model of the battery and bidirectional buck-boost converter.

The DC/DC converter was used to increase the voltage value from about 400V to a constant value of 600V. It was designed to compensate for the voltage drop resulting from the battery discharging while driving. The converter consists of two IGBT transistors, which are switched on alternately at intervals determined by the control system. When the lower transistor is switched on, current flows only through the series connection of inductance L2 and a resistor, reflecting the resistance of the element. The low impedance of the circuit makes a current of significant value flow through the coil. When the lower transistor is switched off and the upper one is switched on, the current begins to flow through the current path of the inverter and the motor windings. From the laws of commutation, it follows that the value of the current flowing through the coil cannot vary by leaps and bounds, which causes the voltage present at the motor terminals to have an increased value. The system is controlled by changing the pulse width factor, that is, by changing the ratio of the transistors' switching times. It is calculated based on the value of the measured voltage and takes into account its drop and allows for its partial compensation. It is necessary to shunt the compensation circuit when starting the system and precharging the capacitors (Bodo et al., 2017; Diab et al., 2016; Gong and Xiong, 2014; Hayes and Davis, 2014).

## 6. Vector Control Systems

In this study, two vector control systems with a six-phase induction motor are considered: the direct field-oriented control (DFOC) method and the direct torque control with space vector modulator (DTC-SVM) with the twelve-sector space vector modulator (Frikha et al., 2023; Levi et al., 2007; Orłowska-Kowalska, 2003; Taha et al., 2022). Based on the tests and the characteristics of the tested structures, the best one was determined, which was analysed later in this study.

The block scheme of the DFOC control system with a six-phase induction motor is shown in Figure 6.

In the direct field-oriented control structure, the rotor flux position angle ( $x$ -axis of the rotating coordinate system), measured with respect to the  $\alpha$ -axis ( $A$ -phase axis of the stator) of the rectangular coordinate system, is determined by a system that reconstructs the components of the rotor flux vector based on the measurement of motor currents and voltages using the MRAS<sup>F</sup> estimator. For the DFOC method, a rotating  $x$ - $y$  coordinate system is used. It is assumed that the rotor flux vector is oriented along the  $x$ -axis, and the current vector is oriented with

respect to the rotor flux vector, shifted with respect to it by the load angle ( $\delta$ ) and spins synchronously with the field represented by the rotor flux. The rotor flux in the machine is controlled by the  $x$  component of the stator current vector. The electromagnetic torque is controlled by changing the  $y$  component of the stator current vector, taking into account that it also depends on the rotor flux. The rotor flux must be stabilised to maintain a linear relationship between this component and the torque.

The DFOC scheme consists of four control loops. The first outer control loop regulates the motor speed, and the second outer control loop regulates the magnitude of the rotor flux vector. The  $x$  component of the stator current vector is determined by the PI controller of magnitude of the rotor flux vector, and the  $y$  component of the stator current vector is determined by the PI speed controller. The both inner control loops with PI controllers regulate values of the  $x$  and  $y$  components of the stator current vector. The output control signals from these controllers determine the reference components of the stator voltage vector in the  $x$ - $y$  coordinate system. In addition to the controllers, the structure includes elements that implement Clarke and Park transformations, the space vector modulator, the MRAS<sup>F</sup> estimator, the flux setter and voltage source inverter (VSI).

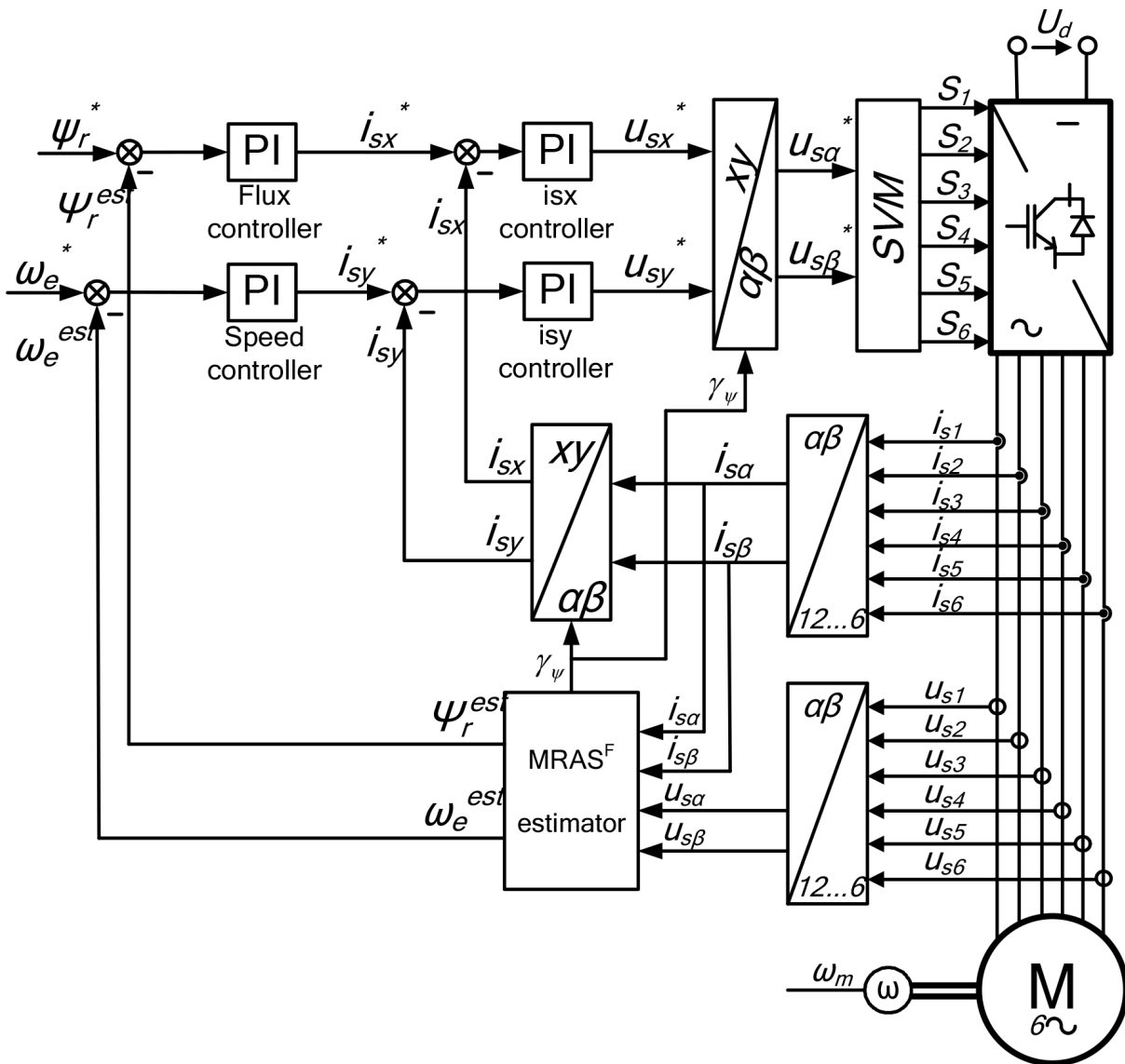
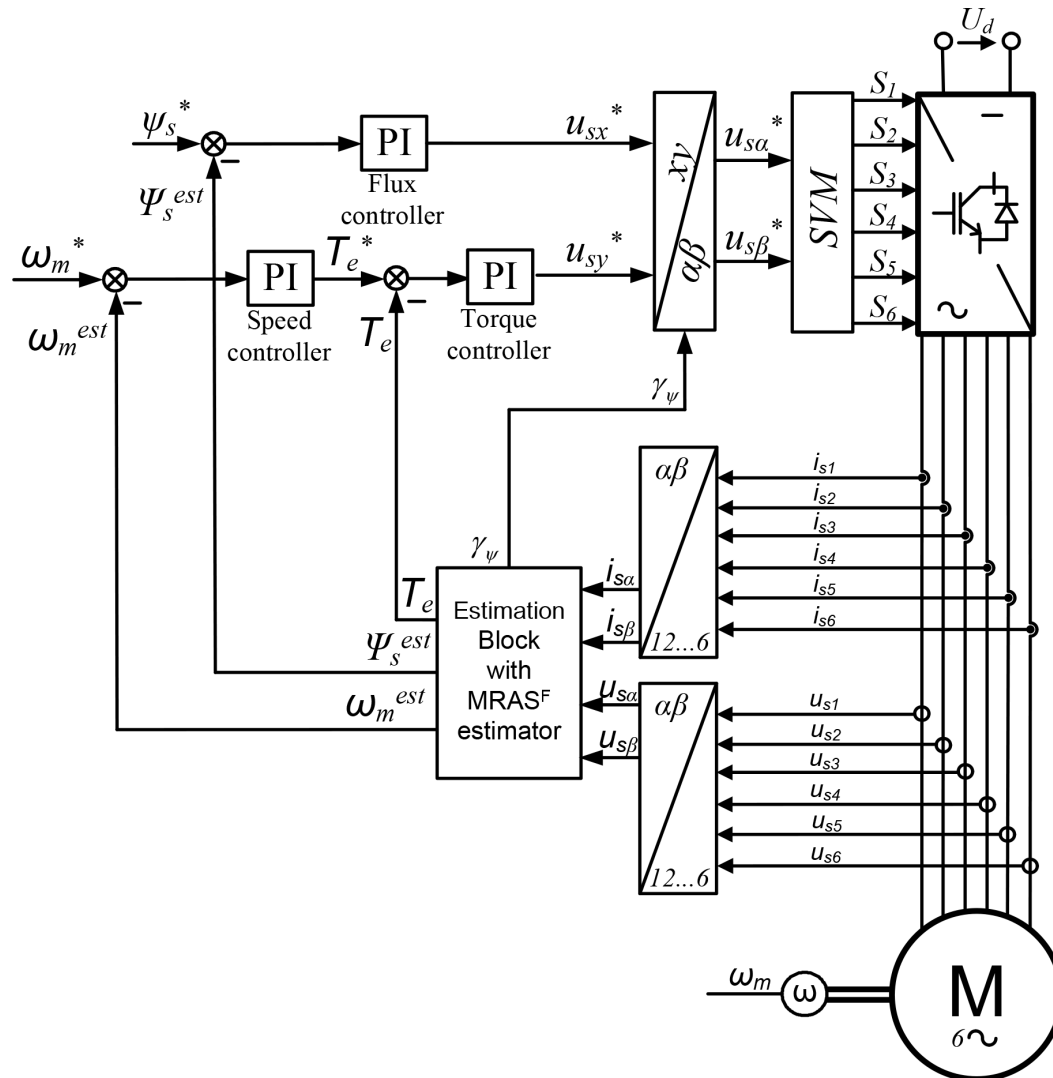


Fig. 6. Block scheme of the DFOC control system with a six-phase induction motor.

The block scheme of the DTC-SVM control system is shown in Figure 7.



**Fig. 7.** Block scheme of the DTC-SVM control system with a six-phase induction motor.

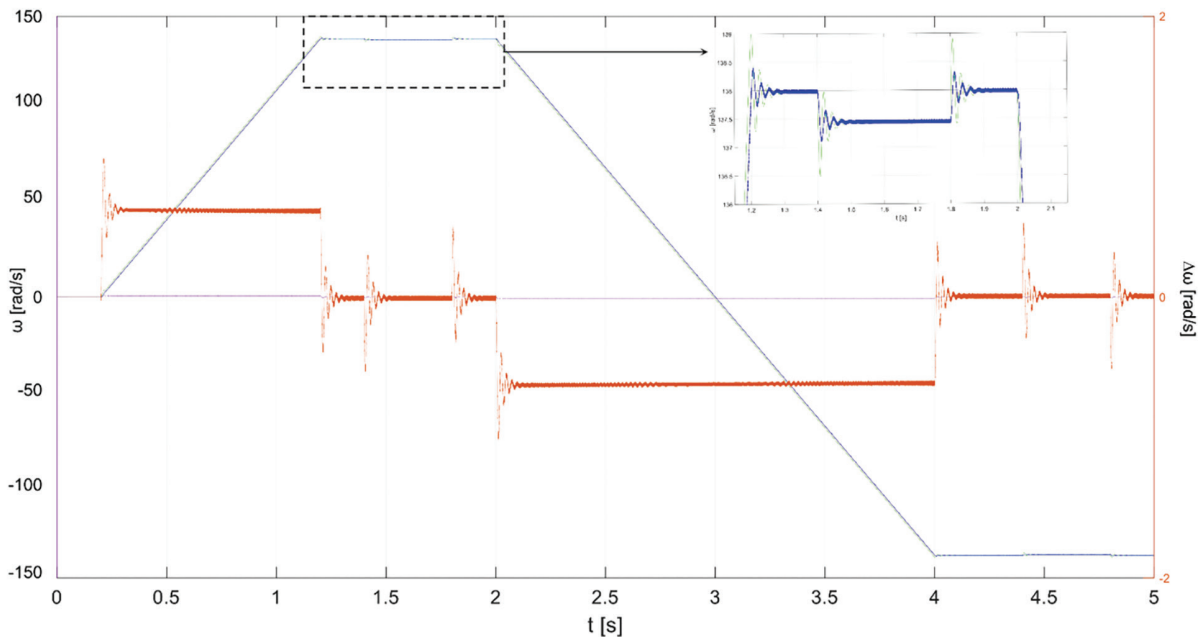
The DTC-SVM control method involves controlling the stator flux vector by changing the stator voltage vector, taking into account that the stator flux is related to the rotor flux. Torque value can be controlled over a wide range by changing only the angle between the aforementioned vectors. The values of the amplitudes of the two fluxes when controlling this angle can remain constant, usually at the nominal level. Changing the stator flux vector is done by changing the voltage vector. After changing the voltage vector, the stator flux vector assumes its position. The voltage is modulated by the inverter, which, for example, in a bridge system of twelve transistors, allows 64 states of the vector for a six-phase motor. Ten of the vector states are extreme positions at which no voltage is applied to the motor (the so-called zero vectors), but they are also applied in the control system. The remaining 54 vectors (active vectors) are equally distributed in the  $\alpha\beta$  plane. The rotor flux vector approaches the stator flux vector, and the angle decreases or increases depending on the direction of the rotation and so does the motor torque. The selection of vectors by the SVM makes it possible to increase and decrease the torque by increasing or decreasing the angle, but also to change its sign when the load angle is greater than 180 degrees. To smooth the torque control, it is necessary to allow the resultant voltage space vector to reach any position on the  $\alpha\beta$  plane. This is done by switching the two positions alternately in different timing configurations (e.g., vector 49 [110001] for 1/3 period time and vector 57 [111001] for 2/3 period time).

The DTC-SVM control system contains three control loops. The flux control loop has a flux controller, and the torque control loop has a master speed controller and a subordinate torque controller. The use of a speed controller improves the characteristics of the system. The stator flux is controlled by the  $x$  component of the stator voltage vector, and the electromagnetic torque is controlled by the  $y$  component of the stator voltage vector. Control of stator flux and motor torque (forcing the  $x$  and  $y$  components of the voltage) is done in the  $x$ - $y$  coordinate system. The rest of the circuit is identical to the DFOC structure.

## 7. Simulation Studies of the DFOC and DTC-SVM Control Systems with a Six-Phase Induction Motor

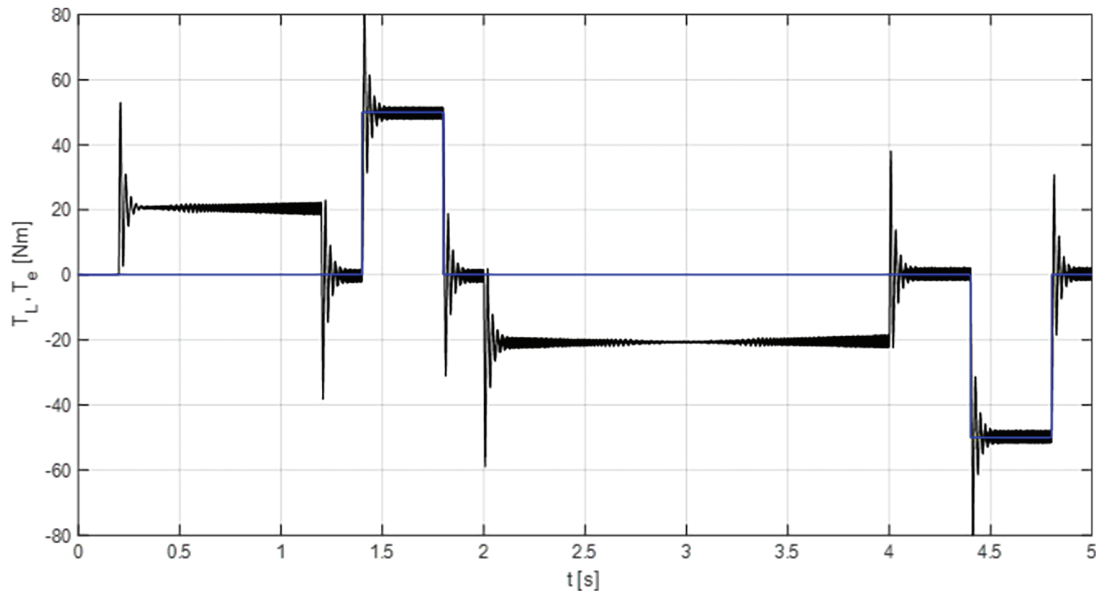
The simulation studies of the DFOC and DTC-SVM control systems were performed in MATLAB-Simulink Software. Simulation studies were carried out for the six-phase squirrel-cage induction motor with following the parameters:  $P_N = 50$  kW,  $U_{fN} = 380$  V,  $I_{fN} = 88$  A,  $f_N = 50$  Hz,  $\omega_{eN} = 276$  rad/s,  $p_b = 2$ ,  $R_s = 0.0645$   $\Omega$ ,  $R_r = 0.0463$   $\Omega$ ,  $L_s = L_{lr} = 0.01$  H and  $L_m = 0.25$  H. The waveforms of the motor speed, electromagnetic torque, load torque and currents when forcing the test speed waveform are presented here. In addition, the hodographs of the rotor flux vector (DFOC) and the stator flux vector (DTC-SVM) are shown. Test speed waveform includes accelerating the motor to rated speed, loading it with a torque of 50 Nm and unloading it at constant speed. Then, the speed reversal is carried out, and the load is engaged and disengaged while running in the other direction. In each of the structures, the flux is stabilised at a constant value. The calculations made from the model are highly accurate; they use five million samples of each physical quantity, which are obtained within 5 seconds of simulation (Oleszczyszyn, 2022).

The estimated value of speed was used in the feedback loop, and the measured value was only for comparison. The results of simulation tests for the DFOC structure are presented later. In Figure 8, the simulation waveforms of the speeds of the six-phase squirrel-cage induction motor for the DFOC control system and the difference between the measured and estimated motor speed are also presented. In the case of the DFOC structure, a speed overshoot of a small value (less than 1%) can be observed. The PI controller settings were selected to achieve good results for the control structure using the MRAS<sup>F</sup> estimator. Extremely high gain values and elimination of the speed error can lead to loss of stability.



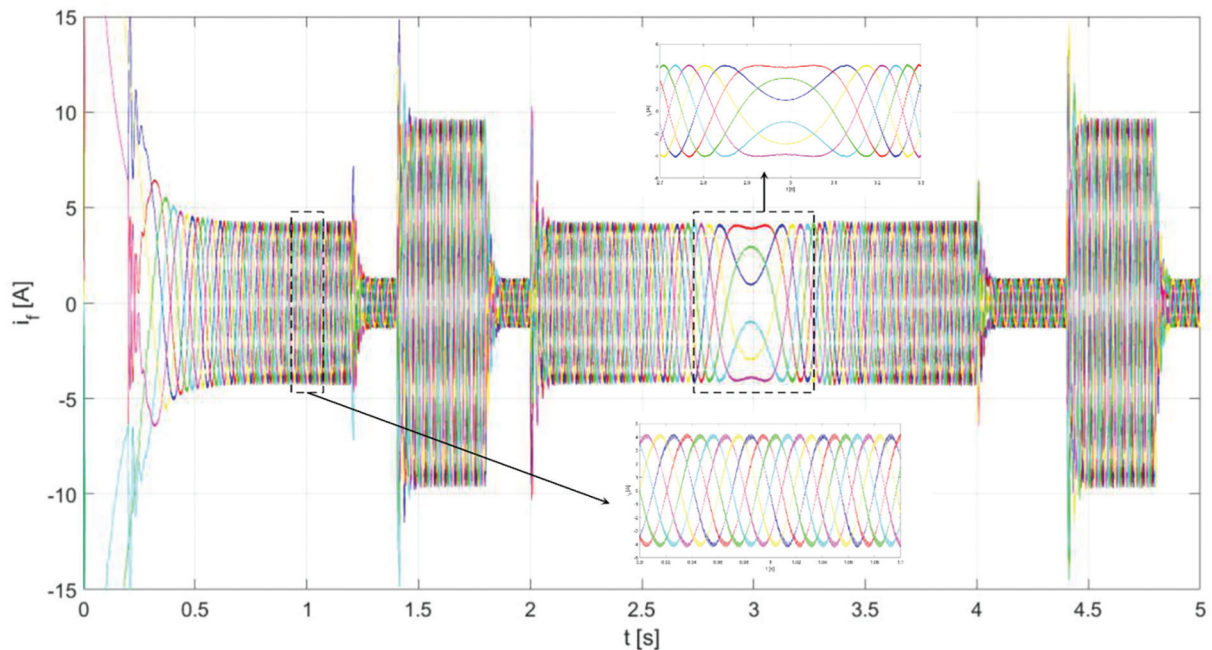
**Fig. 8.** Simulation waveforms of the set motor speed (black), measured motor speed (green), estimated motor speed (blue) and the difference between the measured and estimated speed (orange) of the six-phase squirrel-cage induction motor for the DFOC control system.

The simulation transients of the motor electromagnetic torque and the load torque are presented in Figure 9. The motor torque tracks the set torque very well. After a sudden change in the reference torque, both overshoot and slight oscillation of the motor's electromagnetic torque can be observed. It is caused by the use of the MRAS<sup>F</sup> estimator in the control system. The absolute value of overshoot is at a constant level; it does not depend on the value of the electromagnetic torque or the value of its change.



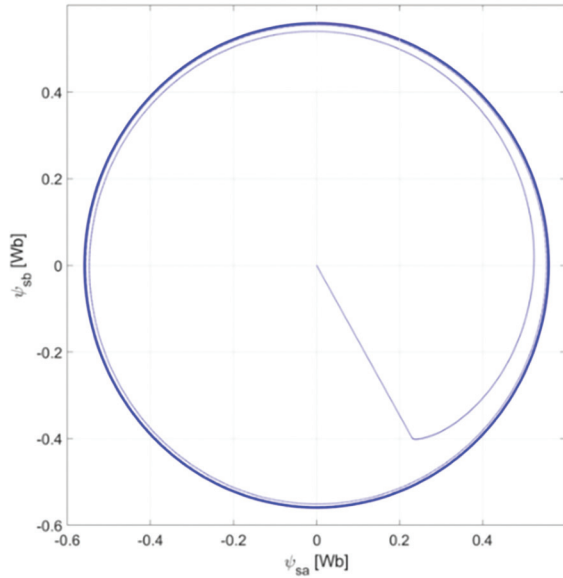
**Fig. 9.** Simulation transients of the electromagnetic torque (black) of the six-phase induction motor and the load torque (blue) for the DFOC control system.

Figure 10 shows the simulation transients of the stator phase currents of the six-phase induction motor for the DFOC control system. Currents in all phases maintain a sinusoidal shape. The values of their amplitudes are the same for all six phases.



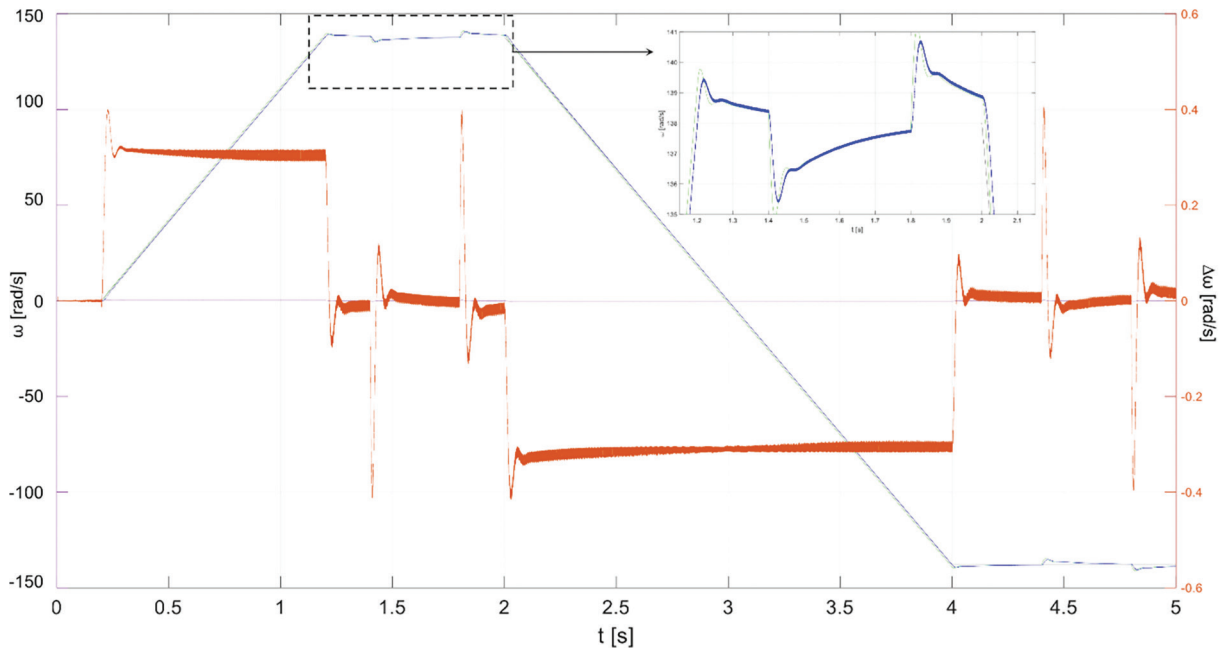
**Fig. 10.** Simulation transients of the stator phase currents of the six-phase squirrel-cage induction motor for the DFOC control system.

Figure 11 shows the hodograph of the rotor flux vector. The trajectory is very even, and its shape almost does not deviate from that of an ideal circle. A line can be seen inside, which reflects the flux build-up during the motor start-up.



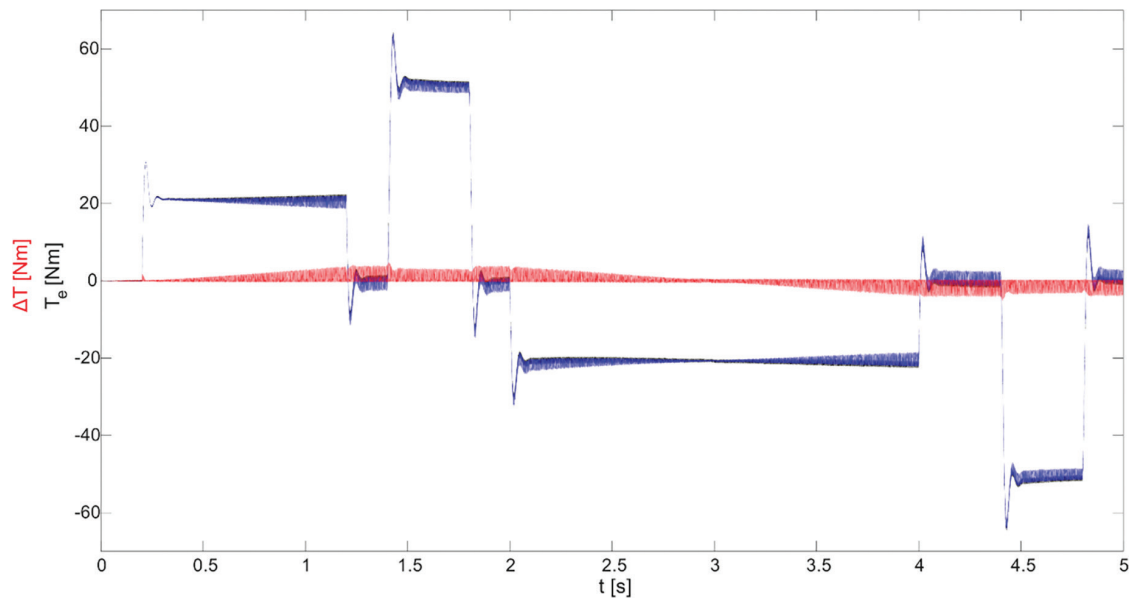
**Fig. 11.** Hodograph of the rotor flux vector of the six-phase induction motor for the DFOC control system.

The results of simulation tests for the DTC-SVM structure are presented here. In Figure 12, the simulation waveforms of the speeds of the six-phase squirrel-cage induction motor for the DTC-SVM control system and the difference between the measured and estimated motor speed are presented. In the case of the DTC-SVM control structure, the overshoot reaches less than 2%, but the deviation decreases to zero with load duration.



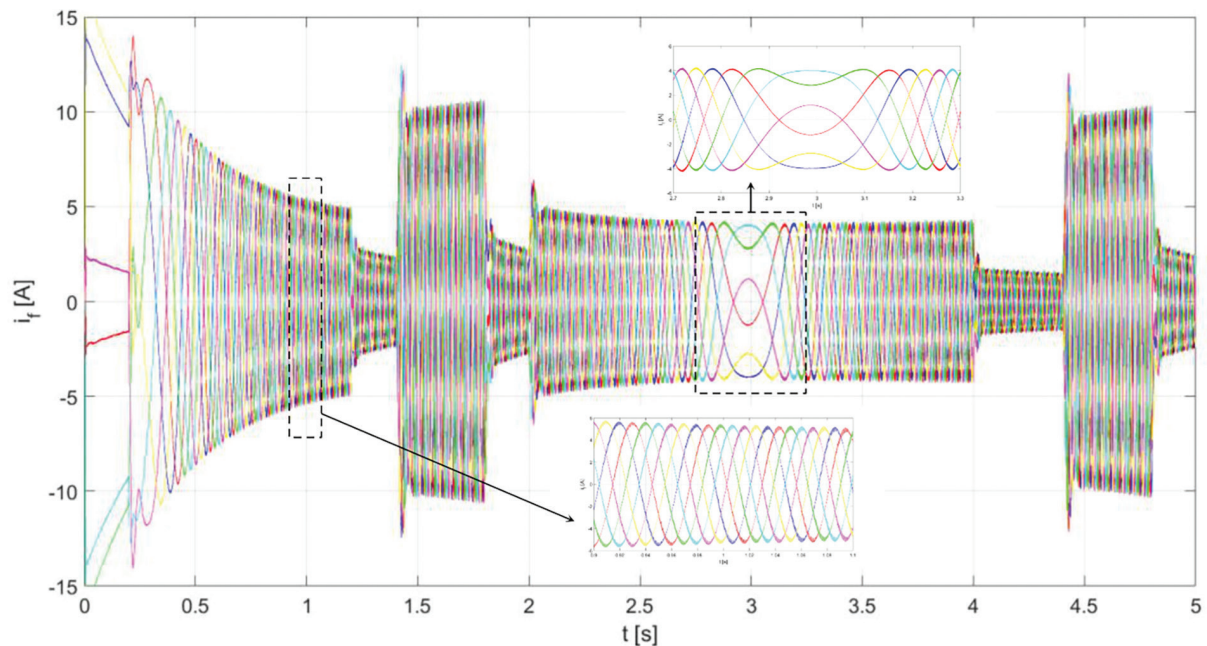
**Fig. 12.** Simulation waveforms of the set motor speed (black), measured motor speed (green), estimated motor speed (blue) and the difference between the measured and estimated speed (orange) of the six-phase squirrel-cage induction motor for the DTC-SVM control system.

The simulation transients of the set motor electromagnetic torque, the measured motor electromagnetic torque and the difference between the set and measured motor electromagnetic torque are presented in Figure 13. The motor torque tracks the set torque very well. After a sudden change in the reference torque, overshoot can be observed, but it has a much smaller value than in the case of the DFOC structure. The absolute value of overshoot depends on the value of the change in the motor's electromagnetic torque.



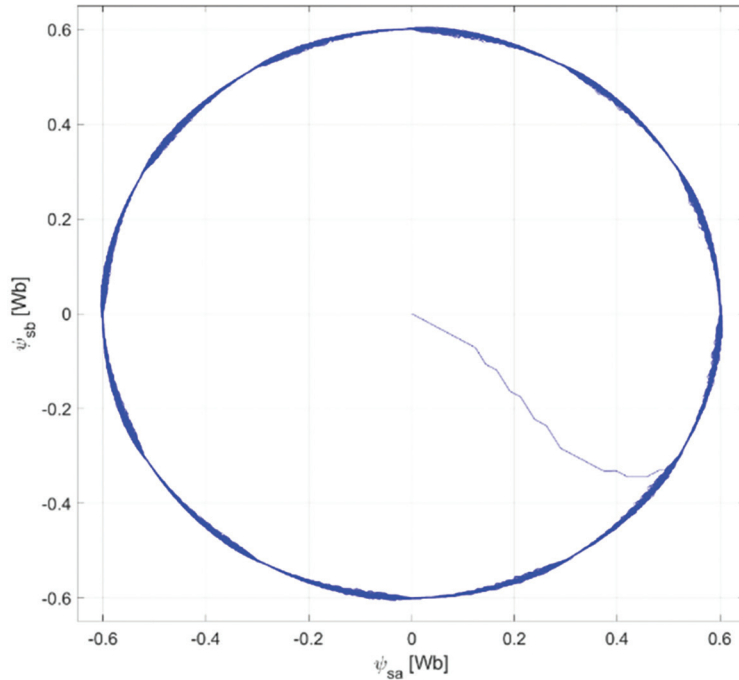
**Fig. 13.** Simulation transients of the set electromagnetic torque (black), the measured electromagnetic torque (blue) and the difference between the set and measured motor electromagnetic torque (red) of the six-phase induction motor for the DTC-SVM control system.

Figure 14 shows the simulation transients of the stator phase currents of the six-phase induction motor for the DTC-SVM control system. In the current waveforms with DTC-SVM control, the smaller oscillations can be observed than with DFOC control. As with the DFOC structure, the amplitudes of the currents for all 6 phases are the same, and the waveforms have sinusoidal shapes, deviating slightly from the ideal due to the switching of the transistors.



**Fig. 14.** Simulation transients of the stator phase currents of the six-phase squirrel-cage induction motor for the DTC-SVM control system.

Figure 15 shows the hodograph of the stator flux vector. On the hodograph of the stator flux vector, it is possible to notice places where its course deviates from the ideal circle. There are 12 such places, which is the same number of sectors used by the vector modulator in the operation of the DTC-SVM structure.



**Fig. 15.** Hodograph of the stator flux vector of the six-phase induction motor for the DTC-SVM control system.

Both analysed structures are characterised by very fast torque response and correct speed control. In each of them, the flux is well stabilised. The smallest fluctuations in the value of the flux coupled to the rotor winding occurring in the DFOC structure. When the motor is loaded at a constant speed, temporary overshoot occurs in both structures. In the field-oriented structure, it has a small value (less than 1%), but there is a speed deviation over the entire range of load operation. In the case of the DTC-SVM structure, the overshoot reaches a value of less than 2%; however, with time, the overshoot decreases and reaches zero. It should be noted that this is on the order of tenths of a second, which means that this phenomenon would have an imperceptible effect on the vehicle's handling.

Because the moment of inertia of the wheels and rotating components while driving was not taken into account in the aforementioned models, the overshoot and associated instantaneous torque shock would be much more limited. Tests taking into account a number of additional parameters and factors are described in the next section.

## 8. Simulation Studies of the Electric Drive System with DTC-SVM Control and a Six-Phase Induction Motor

To illustrate the real operating conditions of the drivetrain as accurately as possible, the engine load was modelled taking into account factors such as air resistance, tire friction resistance and force of gravity acting on a vehicle traveling on an incline. These were determined based on the following formulas (Anderson, 2012):

- Air resistance:

$$F_{aero} = \frac{1}{2} \rho C_d A_f v^2 \quad (23)$$

- Resistance due to the slope of the surface:

$$F_{grade} = mg \cdot \sin(\theta) \quad (24)$$

- Rolling resistance of wheels:

$$F_{rr} = mgC_{rr} \quad (25)$$

where  $m$  is the vehicle mass (1,521 kg);  $g$  is the acceleration of the earth gravitational acceleration ( $9.81 \text{ ms}^{-2}$ );  $\rho$  is the air density (1.225 kg/m<sup>3</sup>);  $C_d$  is the coefficient of drag (0.30);  $A_f$  is the frontal area of the vehicle (2.28 m<sup>2</sup>);  $v$  is the vehicle speed [m/s];  $\theta$  is the roadway slope angle [°]; and  $C_{rr}$  is the coefficient of rolling resistance, determined from the following relation:

$$C_{rr} = 0,005 + \frac{1}{p} (0,01 + 0,0095 \left( \frac{v}{100} \right)^2) \quad (26)$$

where  $p$  is the tire pressure (2.48 bar).

These parameters were selected based on the 2012 Nissan Leaf. For a selected one of the tested structures, tests were carried out to verify the correct operation of the structure in dynamic states. The response of the system to rapid changes of the reference torque while maintaining constant speed was checked, as well as studies on the effect of speed on the accuracy of reference torque tracking.

For the first test, the behaviour of the system was checked for rapid changes in the set torque, but at a constant speed of approximately zero (Oleszczyszyn, 2022). This was achieved by forcing the load torque to the same value as the set motor torque. The purpose of the study is to check the stability of the system when the torque changes rapidly and to check the possible effect of changes in the value of the set torque on its tracking accuracy.

In Figure 16, the simulation transients of the set and measured electromagnetic torque of the six-phase induction motor are presented. In the close-up, it can be seen that the estimated motor torque is equal to the set torque, and its oscillations are hardly noticeable. The waveforms of the reference and estimated magnitude of the stator flux vector are shown in Figure 17.

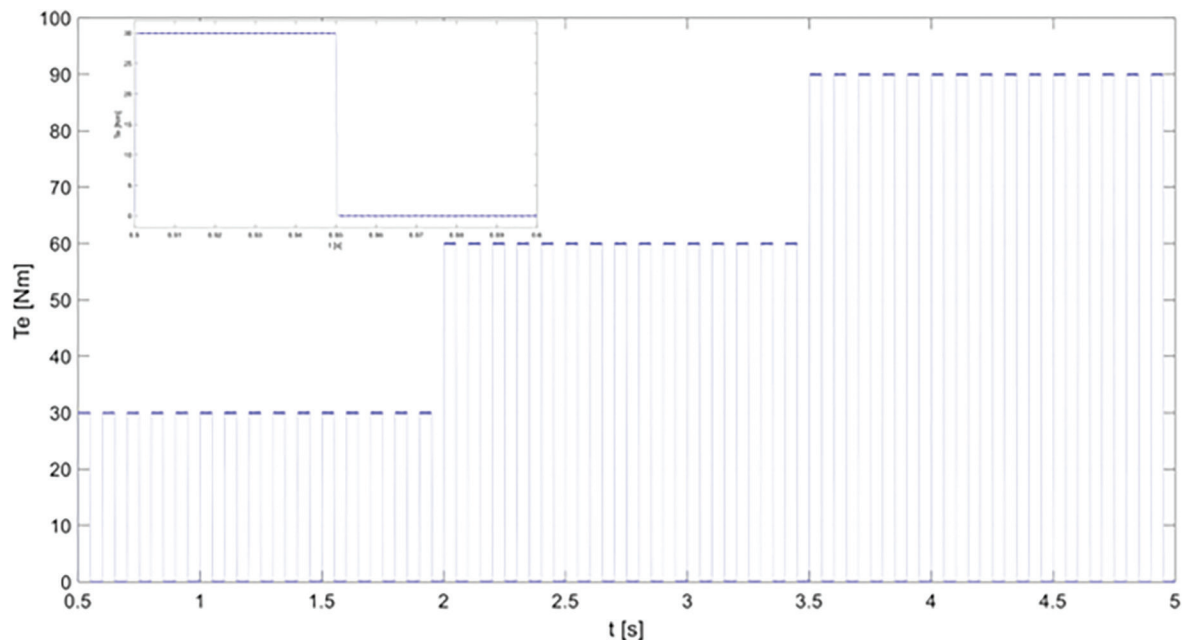


**Fig. 16.** Simulation transients of the set and measured electromagnetic torque of the six-phase induction motor for the DTC-SVM control system.

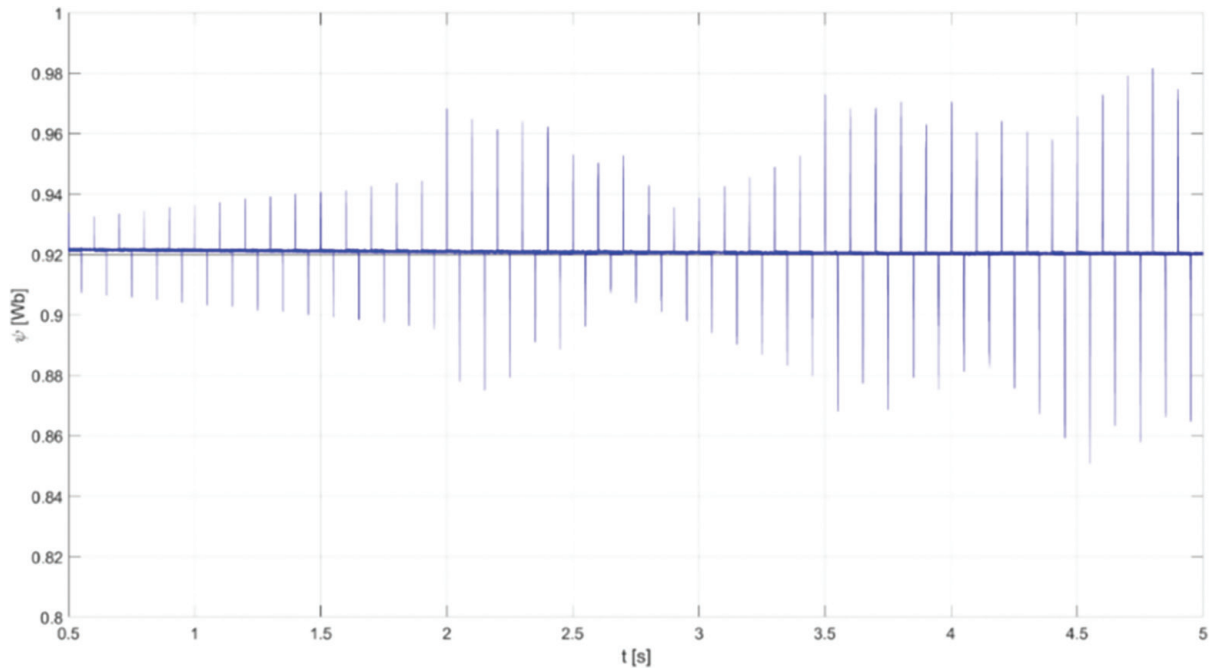


**Fig. 17.** Trajectories of the set (black) and estimated (blue) magnitudes of the stator flux vector of the six-phase induction motor for the DTC-SVM control system.

The system operates stably and shows no signs of tending toward instability. From the torque waveforms in the Figure 16 presented above, it can be seen that the absolute pulsation of the torque is constant for its different values. This indicates that it is due to the inaccuracy of the calculation and the set integration step. If the percentage of pulsation was constant, it could be concluded that this is due to the operation of the system.

The time between forcing the torque and its generation should be noted. It has a value on the order of milliseconds and increases in proportion to the value of the forced torque. The small delays can significantly affect the dynamic capabilities of the vehicle. The dependence of the delay time on the value of the torque is related to the need to force a current, the time constant of which depends on the parameters of the motor (it is small, but non-zero).

The flux associated with the stator winding is maintained at a constant value, close to the setpoint, and in the event of a sudden change in torque, spikes appear in the waveform. Their duration is very short and does not cause negative effects in the operation of the system. Their appearance is due to the fact that the two control paths of the components of the stator voltage vector are coupled to each other; the torque not only depends on the  $y$ -axis component of the stator current but also, to a small extent, on the  $x$ -axis component. An analogous relationship appears in the equation for the flux coupled to the stator winding. To prevent spikes in the flux waveform, it is necessary to use decoupling blocks. In this work, decoupling blocks were not used because they do not have a significant impact on the properties of the modelled vehicle propulsion system.

The second stage of the research was testing the system at variable speed (Oleszczyszyn, 2022). Tests were carried out to determine the effect of engine speed on the accuracy of the system's torque reference tracking. From the data obtained in the previous section, it is clear that there is no need to conduct tests for several different values of the reference torque. Its value has no effect on the oscillations of the electromagnetic torque produced by the motor.

In Figure 18, the simulation waveforms of the speeds of the six-phase squirrel-cage induction motor for the DTC-SVM control system are presented.

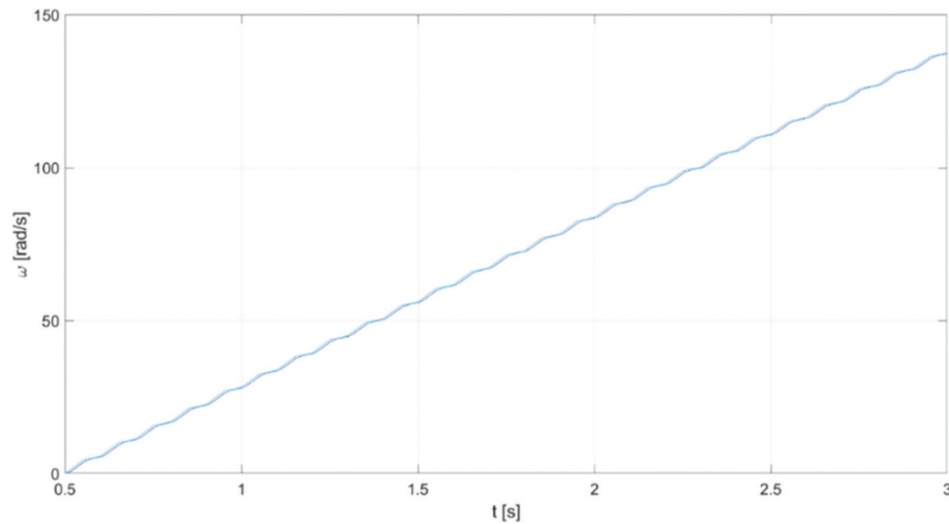


**Fig. 18.** Simulation waveforms of the measured motor speed (light blue) and estimated motor speed (blue) of the six-phase squirrel-cage induction motor for the DTC-SVM control system.

Rapid changes in the set torque were forced into the system with such an adjustment of the load torque that the speed of the system increased approximately linearly. The Figures 19 and 20 presented below show the waveforms of the set torque and torque generated by the motor. Listed are the first and last peaks of the forced torque, corresponding to near-zero speed and near-rated speed. In addition, Figure 21 shows the waveform of the flux vector modulus associated with the motor's stator winding.

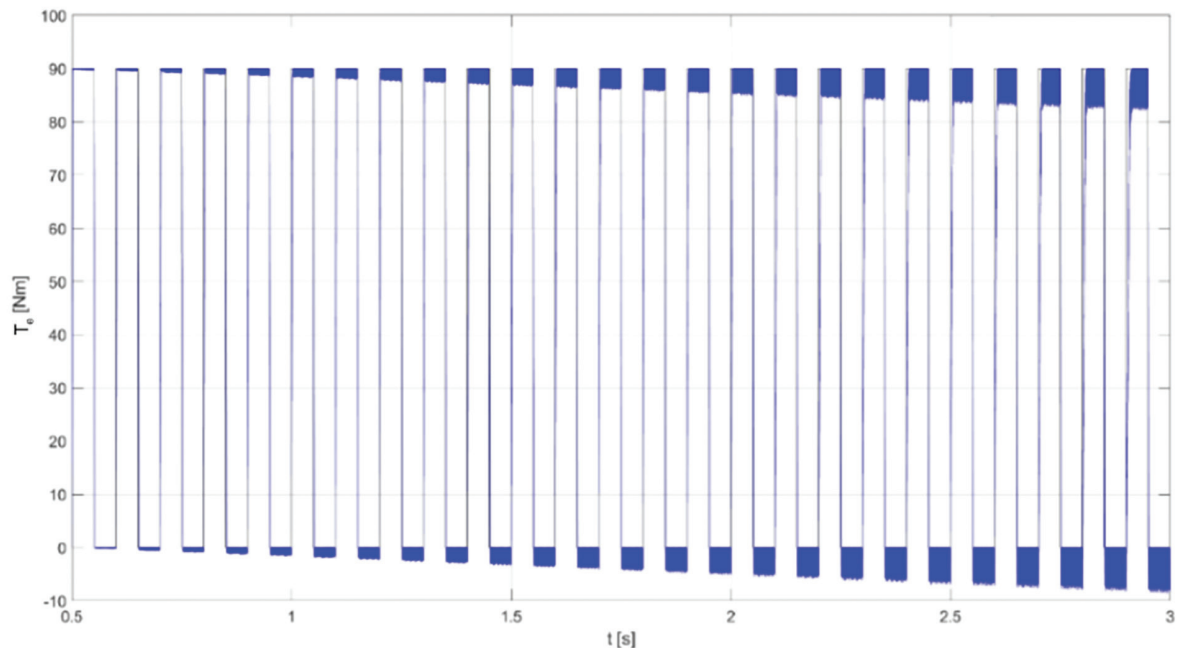


**Fig. 19.** Simulation transients of the set (black) and the measured (blue) electromagnetic torque of the six-phase induction motor for the DTC-SVM control system.

The pulsation of the electromagnetic torque increases as the motor speed increases. This is probably due to the vector modulator's recalculation of vector switching times being too low or by the induced voltage. Unfortunately, increasing this time would make the time of running a 3-second simulation several hours. The dependence of the drive system's response time on its speed should be noted. In the case of the first peak, the time from the forcing

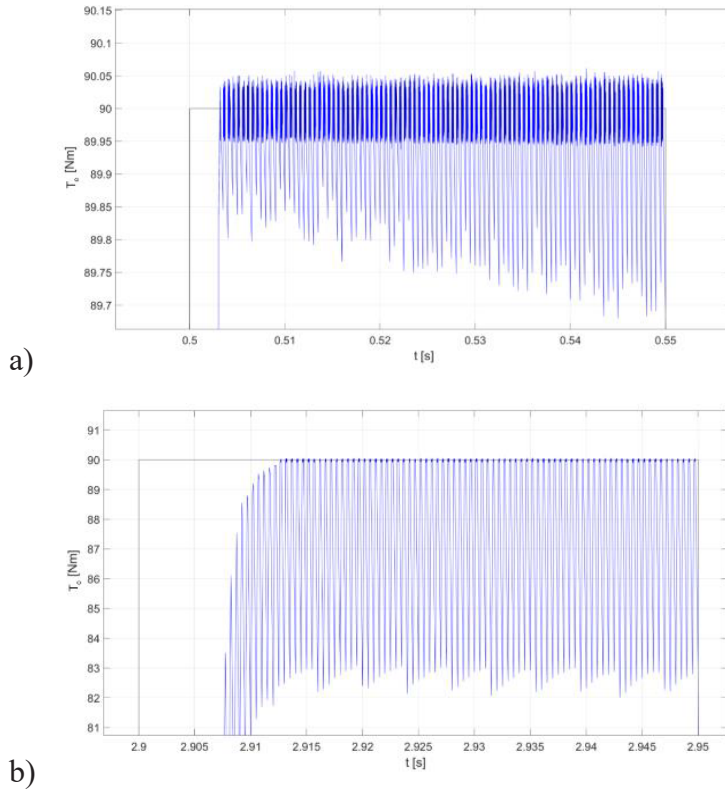


**Fig. 20.** Zooms a) of the first peak of the forced torque; b) of the last peak of the forced torque.

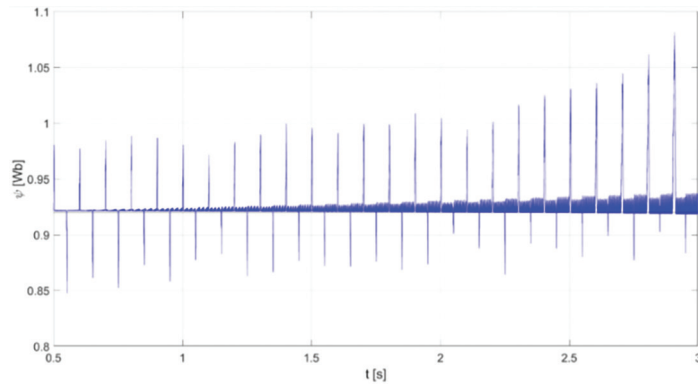


**Fig. 21.** Trajectories of the set (black) and the estimated (blue) magnitude of the stator flux vector of the six-phase induction motor for the DTC-SVM control system.

of the 90 N set signal to its achievement by the system is 3.2 ms, and in the case of the last peak, it is 12.7ms. The pulsation of the motor torque undoubtedly contributes to this.

The speed of the motor also affects the amplitudes of the spikes occurring in the flux waveform. Their occurrence is probably related to the operation of the estimator. The current part is tuned by the estimated speed, so as the speed increases, the amplitudes of the spikes are also increased.

The final point of the research is the simulation of cruise control operation (Oleszczyszyn, 2022), that is, the combination of torque and speed control in a closed control loop. It replicates actual driving in an electric car and involves controlling torque (by pressing the accelerator pedal) until the desired speed is reached and then closing the speed coupling loop (engaging cruise control).

The test involved accelerating from a standstill to a set speed (50km/h and 90km/h), then switching on cruise control and stabilising the constant speed value. The control switchover takes place as soon as the system reaches

the engine speed corresponding to the set speed. During the conducted test, the engine shaft was loaded with the torque resulting from the calculated driving resistance.

In Figure 22, the simulation waveforms of the set vehicle speed and estimated vehicle speed are presented. The speed is regulated very precisely, and the overshoot after reaching the set speed is very small.

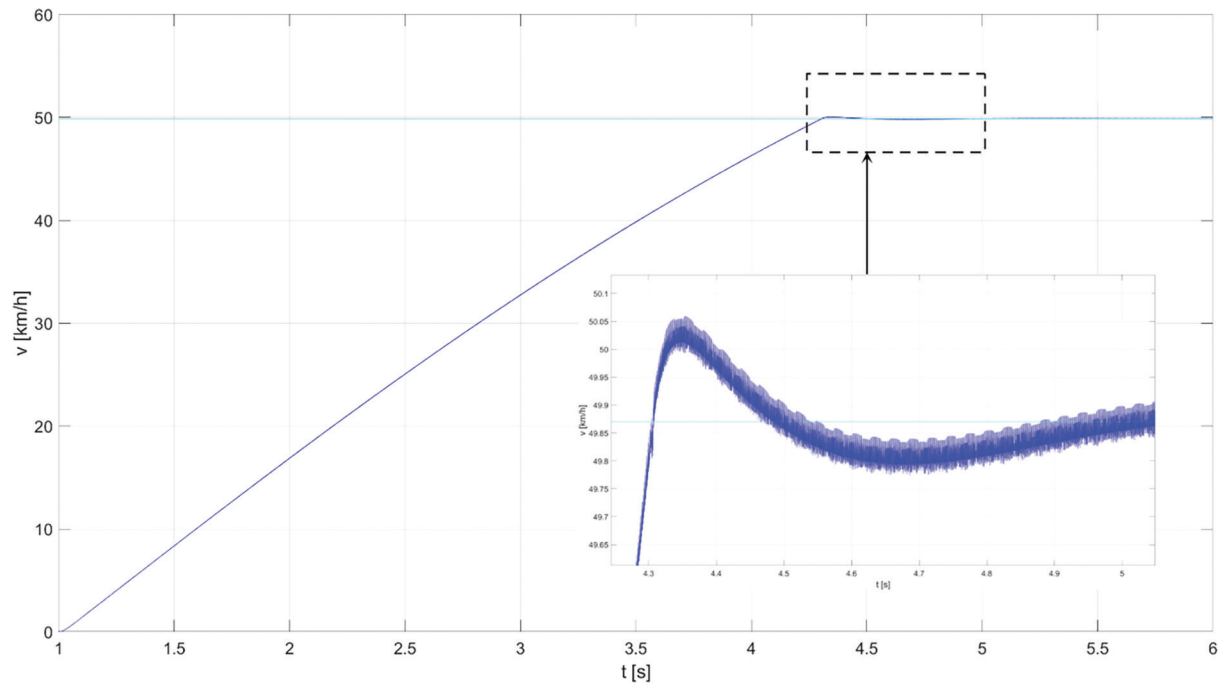


**Fig. 22.** Simulation waveforms of the set vehicle speed (light blue) and estimated vehicle speed (blue).

In Figure 23, the simulation waveforms of the reference torque, motor electromagnetic torque and load torque are presented.

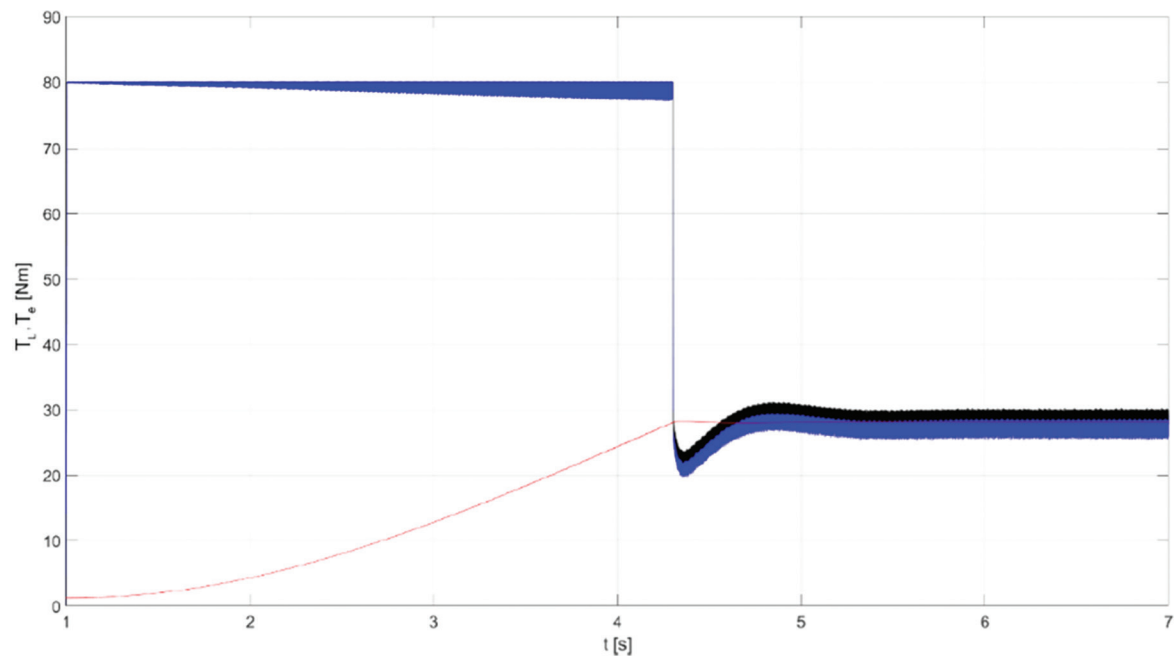


**Fig. 23.** Simulation transients of the reference (black), measured (blue) electromagnetic torque and load (red) torque.

For a set speed of about 50km/h, there is no oscillation or overshoot (its value is on the order of 0.5%). The system smoothly transitions from motor electromagnetic torque control to motor speed control. Closing the speed feedback loop does not bring additional unwanted effects to the system. The set torque is well tracked under both conditions.

Figures 22-23 show the transients of engine speed, torque and vehicle speed when the cruise control is set to a speed of approx. 50 km/h. The Figures 24 and 25 refer to the speed of 90 km/h.

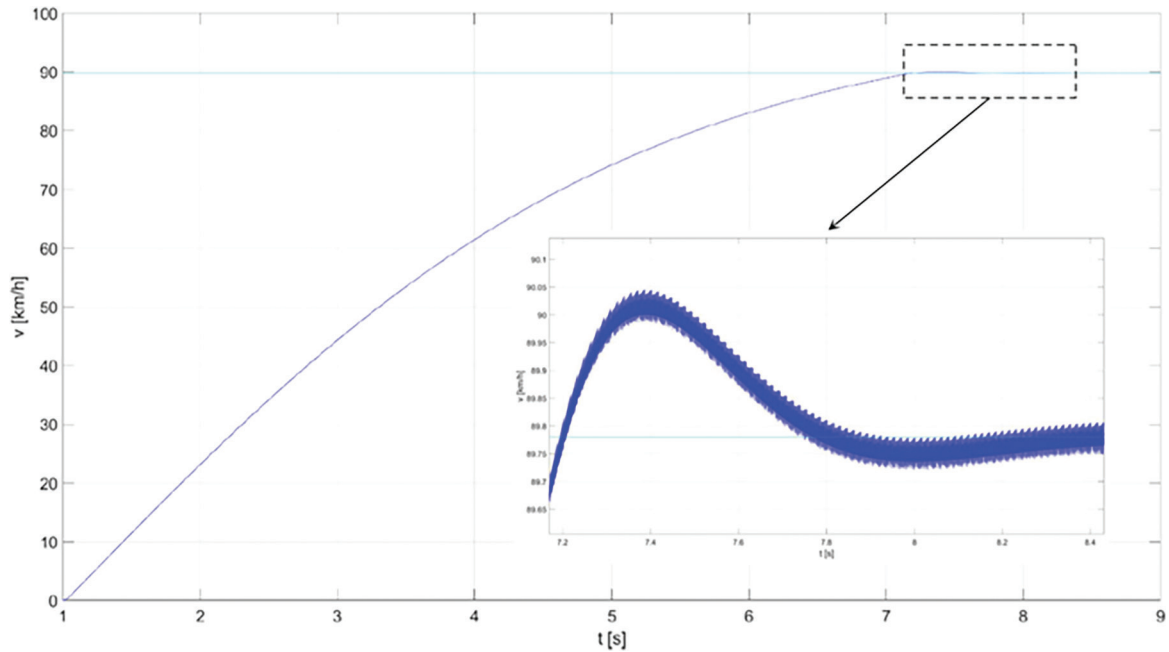


**Fig. 24.** The simulation waveforms of the set vehicle speed (light blue) and estimated vehicle speed (blue).

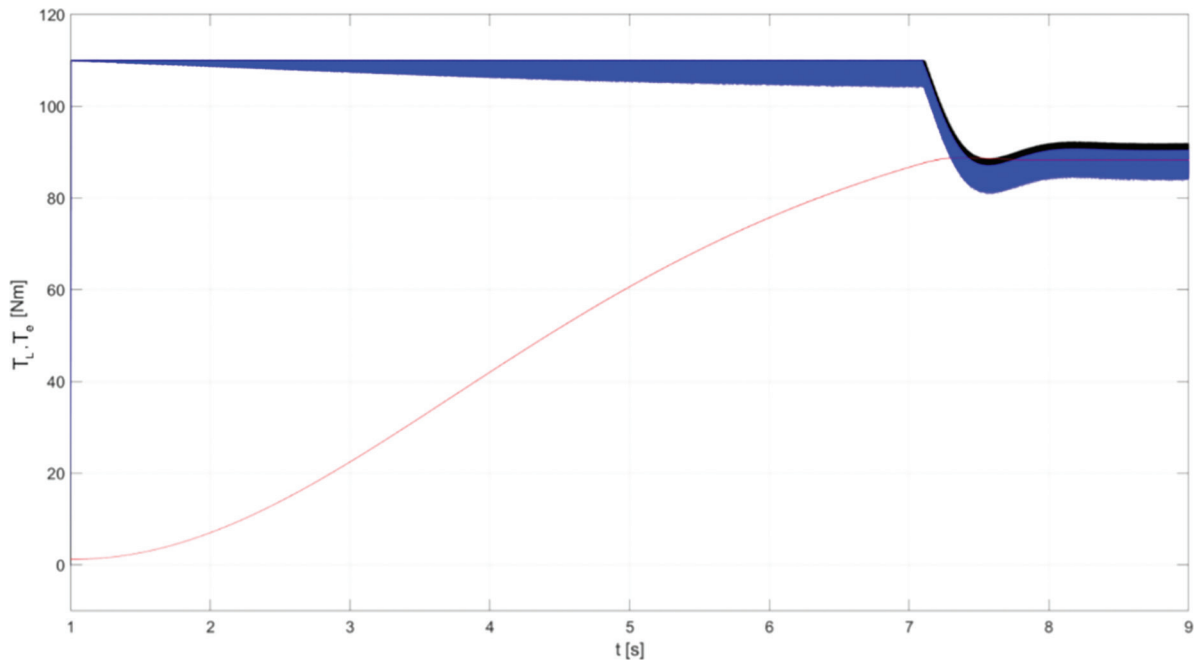


**Fig. 25.** Simulation transients of the reference (black), measured (blue) electromagnetic torque and load (red) torque.

For speeds of about 90 km/h, similar conclusions can be drawn as for speeds of 50 km/h. Both the speed and torque reference waveforms are well reproduced by the actual values.

The modelled engine control system tracks both set torque and speed very well. The overshoots occurring in the speed and torque waveforms have small values and do not affect driving comfort. The DTC-SVM structure is well suited for controlling both the torque and speed of an electric vehicle.

## 9. Conclusions

Drive systems controlled by vector control methods enable control of the electromagnetic torque in both static and dynamic states. The DTC-SVM control structure allows the direct torque control, while giving the ability to work with cruise control by the closing the speed control loop. Torque applied by the driver or cruise control is tracked with high accuracy, and errors arising from changes of the load torque are compensated within tenths of a second. The use of the speed estimator increases the reliability of the drive system in the event of damage to the speed sensor in the vehicle. The DTC-SVM control structure does not contain any significant disadvantages, which makes it an ideal solution for driving electric vehicles.

Modelling a time-varying load made it possible to test the system in conditions close to real. Due to the fact that the mapping of the driver's behaviour is complicated, driving simulation with direct torque control was not carried out, but only the system's capabilities and its stability in this operating state were checked. The step torque forcing (dynamic operation of the accelerator pedal) leads to step changes in the value of the electromagnetic torque without the occurrence of overshoots and deviations. In additions, the time to reach the full electromagnetic torque of the motor is on the order of several milliseconds. These observations confirm the excellent dynamic properties of the control system in the case of direct torque forcing.

Modelling the system with a closed control loop of the motor speed made it possible to recreate road conditions without the need to simulate the behaviour of the driver. In addition, by calculating the load torque associated with air resistance, tire friction and slope, it was possible to check the system's operation in real-life conditions. Switching the mode from torque control to the speed control can take place at any vehicle speed. The system can automatically both accelerate and slow down to achieve the set speed. This feature can be very important in the case of partially or fully autonomous vehicles.

## References

- Anderson, R. (2012). *Online Estimation of Rolling Resistance and Air Drag for Heavy Duty Vehicles*. Master of Science Thesis, KTH Industrial Engineering and Management, Stockholm.
- Bednarz, S. and Dybkowski, M. (2019). Induction Motor Windings Faults Detection Using Flux-Error Based MRAS Estimators. *Diagnostyka*, 20, pp. 87–96.
- Bodo, N., Levi, E., Subotic, I., Empringham, L. and Johnson C. M. (2017). Efficiency Evaluation of Fully Integrated On-Board EV Battery Chargers with Nine-Phase Machines. *IEEE Transactions on Energy Conversion*, vol. 32(1), pp. 257–266.
- Che, H. S., Duran, M. J., Levi, E., Jones, M., Hew, W. P. and Rahim, N. A. (2014). Postfault Operation of an Asymmetrical Six-Phase Induction Machine with Single and Two Isolated Neutral Points. *IEEE Transactions on Power Electronics*, 29(10), pp. 5406–5416.
- Diab, M. S., Elserougi, A. A., Abdel-Khalik, A. S., Massoud, A. M. and Ahmed, S. (2016). A Nine-Switch-Converter-Based Integrated Motor Drive and Battery Charger System for EVs Using Symmetrical Six-Phase Machines. *IEEE Transactions on Industrial Electronics*, 63(9), pp. 5326–5335.
- Frikha, M. A., Croonen, J., Deepak, K., Benomar, Y., El Baghdali, M. and Hegazy, O. (2023). Multiphase Motors and Drive Systems for Electric Vehicle Powertrains: State of the Art Analysis and Future Trends. *Energies*, 16(2), pp. 768–813.
- Gong, X. and Xiong, R. (2014). Study of the Characteristics of Battery Packs in Electric Vehicles with Parallel-Connected Lithium-Ion Battery Cells. *IEEE Transactions on Industry Applications*, 51, pp. 1872–1879.
- Guziński, J. and Adamowicz, M. (2013). Drive Systems in Electric Vehicle. *Automatyka-Elektryka-Zakłócenia*, 3, pp. 64–75 (in Polish).
- Hayes, J. and Davis, K. (2014). Simplified Electric Vehicle Powertrain Model for Range and Energy Consumption Based on EPA Coast-Down Parameters and Test Validation by Argonne National Lab Data on the Nissan Leaf. *2014 IEEE*

- Transportation Electrification Conference and Expo (ITEC)*, June 2014, Michigan, USA.
- Korzonek, M., Tarchała, G. and Orłowska-Kowalska, T. (2019). A Review on MRAS-Type Speed Estimators for Reliable and Efficient Induction Motor Drives. *ISA Trans*, 93, pp. 1–13.
- Levi, E., Bojoi, R., Profumo, F., Toliyat, H. A. and Williamson, S. (2007). Multiphase Induction Motor Drives – A Technology Status Review. *IET Electric Power Application*, 1(4), pp. 489–516.
- Listwan, J. (2019). Analysis of Fault States in Drive Systems with Multi-Phase Induction Motors. *Archives of Electrical Engineering*, 68(4), pp. 817–830.
- Listwan, J. and Pieńkowski, K. (2016). Direct Field-Oriented Control of Six-Phase Induction Motor with Fuzzy-Logic Speed Controller. *Power Electronics and Drives*, 1(36), pp. 91–101.
- Łebkowski, A. (2017). Exploitation Tests of an Electric Powertrain for a Light Electric Vehicle. *Scientific Journal of Gdynia Maritime University*, 98, pp. 139–147 (in Polish).
- Łebkowski, A. (2017). Light Electric Vehicle Powertrain Analysis. *Scientific Journal of Silesian University of Technology. Series Transport*, 94, pp. 123137.
- Munim, W.N.W.A., Duran, M.J., Che, H.S., Bermudez, M., Gonzales-Prieto, I. and Rahim, N. A., (2017). A Unified Analysis of the Fault Tolerance Capability in Six-Phase Induction Motor Drives. *IEEE Transactions on Power Electronics*, 29(10), pp. 7824–7836.
- Novotny, D. W. and Lipo, T. A. (1996). *Vector Control and Dynamics of AC Drives*. Oxford University Press.
- Oleszczyszyn, P. (2022). *Analysis of the Drive of the Electric Vehicle with Six-Phase Induction Motor*. Master of Science Thesis, Faculty of Electrical Engineering, Wrocław University of Science and Technology (in Polish).
- Orłowska-Kowalska, T. (2003). *Sensorless Induction Motor Drives*. Wrocław University of Technology Press (in Polish).
- Strankowski, P., Guziński, J., Wilczyński, F., Morawiec, M. and Lewicki, A. (2019). Open-Phase Fault Detection Method for Sensorless Five-Phase Induction Motor Drives with an Inverter Output Filter. *Power Electronics and Drives*, 4(39), pp. 189–200.
- Sztafrowski, D. and Kaznowski, R. (2021). Infrastructure Problems Related to the Transition from Internal Combustion to Electric Drive in Motor Vehicles. *Przegląd Elektrotechniczny*, 4, pp. 113–116 (in Polish).
- Taha, W., Azer, P., Dorneles Callegaro, A. and Emadi, A. (2022). Multiphase Traction Inverters: State of the Art Review and Future Trends. *IEEE Access*, 10, pp. 4580–4599.
- Zachariasz, M. and Dybkowski, M. (2014). Analysis of Hybrid Electrical Vehicle with Induction Motor. *Scientific Papers of the Institute of Electrical Machines, Drives and Measurements of the Wrocław University of Technology*, 34, pp. 225–232 (in Polish).